

Article

Experimental Tests and Aeroacoustic Simulations of the Control of Cavity Tone by Plasma Actuators

Hiroshi Yokoyama * , Isamu Tanimoto and Akiyoshi Iida

Department of Mechanical Engineering, Toyohashi University of Technology, Toyohashi 441-8580, Japan; tanimoto@aero.me.tut.ac.jp (I.T.); iida@me.tut.ac.jp (A.I.)

* Correspondence: h-yokoyama@me.tut.ac.jp; Tel.: +81-532-44-6665

Received: 18 July 2017; Accepted: 3 August 2017; Published: 4 August 2017

Featured Application: Noise reduction in high-speed transport vehicles.

Abstract: A plasma actuator comprising a dielectric layer sandwiched between upper and lower electrodes can induce a flow from the upper to lower electrode by means of an externally-applied electric field. Our objective is to clarify the mechanism by which such actuators can control the cavity tone. Plasma actuators, with the electrodes elongated in the streamwise direction and aligned in the spanwise direction, were placed in the incoming boundary of a deep cavity with a depth-to-length ratio of 2.5. By using this experimental arrangement, the amount of sound reduction (“control effect”) produced by actuators of differing dimensions was measured. Direct aeroacoustic simulations were performed for controlling the cavity tone by using these actuators, where the distributions of the body forces applied by the actuators were determined from measurements of the plasma luminescence. The predicted control effects on the flow and sound fields were found to agree well with the experimental results. The simulations show that longitudinal streamwise vortices are introduced in the incoming boundary by the actuators, and the vortices form rib structures in the cavity flow. These vortices distort and weaken the two-dimensional vortices responsible for producing the cavity tone, causing the tonal sound to be reduced.

Keywords: cavity tone; direct aeroacoustic simulation; aeroacoustics; plasma actuators; flow control; noise control; vortices; wind tunnel experiments; acoustic sources

1. Introduction

Self-sustained oscillations in a flow over a cavity as shown in Figure 1—such as a sunroof of an automobile or various gaps between parts of a high-speed transportation vehicle—can radiate intense tonal noise as a cavity tone. This high-intensity noise also occurs at a single peak frequency, making it a very unpleasant for many people. It is, thus, important to develop methods to suppress such cavity tones.

Many researchers over the past 50 years have investigated the mechanism of acoustic radiation from self-sustained oscillations in cavity flows. Rossiter [1] described an oscillation mechanism similar to that presented for edge tones by Powell [2]. In this mechanism, the interactions of vortices with the downstream edge of the cavity radiate acoustic waves, which cause the formation of new vortices at the upstream edge. Furthermore, an acoustic resonance sometimes occurs in the cavity—such as a one-quarter-wavelength-depth mode—making the cavity tone more intense [3].

Zhuang et al. [4] investigated the control of the cavity tone by blowing jets at the upstream edge of the cavity. Yokoyama et al. [5] showed that the cavity tone can be reduced by blowing jets aligned across the span in the upstream boundary layer, and the amount of reduction was affected by the spacing of the jets.

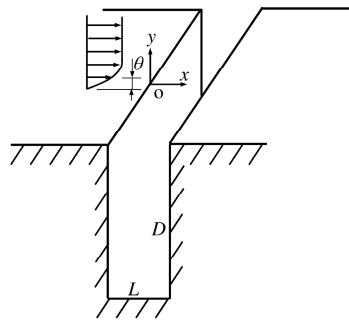


Figure 1. Configuration of the flow over a cavity.

Control of the cavity tone by a plasma actuator (PA) has also been investigated [6,7]. Figure 2 shows a typical configuration of a dielectric-barrier-discharge plasma actuator. It comprises an upper exposed and a lower embedded electrode, with a dielectric layer sandwiched between the electrodes. By applying a high AC voltage to the electrodes, momentum is transferred from the charged plasma particles to the neutral gas through collisions between the plasma components and neutral air molecules. As a result, a flow is induced from the upper electrode toward the lower one. Plasma actuators have many advantages: they are simple configurations without moving parts, have fast time response and low mass, with the ability to be attached easily onto objects, as compared with other flow-control actuators, such as a piezo-actuator, an impinging jet, or a synthetic jet.

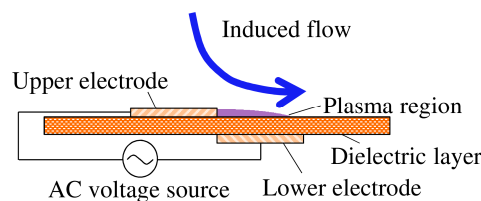


Figure 2. Typical configuration of a dielectric-barrier-discharge plasma actuator.

Huang et al. [6] succeeded in reducing the cavity tone by using spanwise-aligned plasma actuators, with the electrodes elongated in the streamwise direction (“streamwise plasma actuators”), which introduced a spanwise variation of velocity in the cavity flow. However, the sound-reduction mechanism of this approach has not been clarified in detail.

The objective of the present investigation is to clarify the mechanism by which streamwise plasma actuators reduce the cavity tone. In preliminary experiments, the effects of the spanwise width and pitch of the lower electrode on the control of the cavity tone were studied. In Section 2, both our experimental methodologies and the simulations performed to clarify the mechanism through which the plasma actuators control the intensity of the cavity tone are discussed. The comparison of predicted results with those measured is discussed in Section 3. The predicted and measured results are discussed in detail in Section 4. In Section 5, conclusions are summarized.

2. Methodologies

2.1. Experimental Tests

2.1.1. Wind Tunnel and Test Section

Figure 3 shows the experimental setup for our tests. The experiments were carried out using a suction-type, low-noise wind tunnel with a rectangular test section having a cross-section with dimensions of 150 mm × 75 mm. The intensity of freestream turbulence was less than 0.5%, and the background-noise level was 55.2 dB (A) at the freestream velocity of 30 m/s.

$\theta/L = 0.0071$ for a freestream velocity of $U_0 = 30$ m/s at the upstream edge of the cavity, where this value was measured and found to be consistent with that predicted for flow over a flat plate without a cavity.

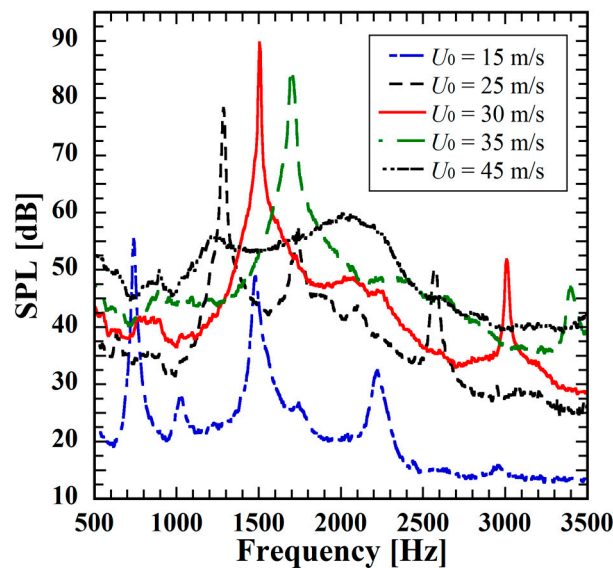


Figure 4. Measured sound-pressure spectra without control at $U_0 = 15, 25, 30, 35, 45$ m/s. SPL is the sound-pressure level in decibels

2.3. Plasma Actuator Control

2.3.1. Control by Streamwise Plasma Actuators

As shown in Figure 5, the plasma actuators consist of lower and upper copper electrodes $18 \mu\text{m}$ thick, with a dielectric layer of polyimide $200 \mu\text{m}$ thick sandwiched between them. The lower electrodes were placed in the spanwise direction between the upper electrodes. The actuators were designed and built by the authors. As discussed in Section 3.1, these actuators induce pairs of streamwise vortices with spanwise widths equal to those of the lower electrodes. The electrodes were arranged symmetrically in the spanwise direction with respect to the mid-span ($z = 0$).

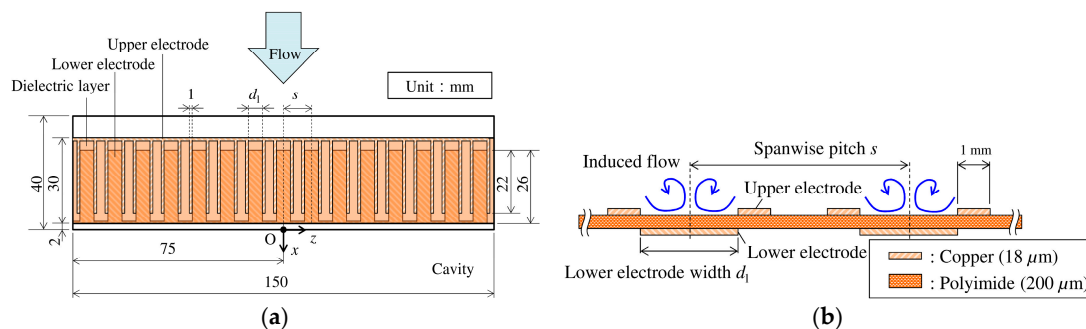


Figure 5. Configuration of the streamwise plasma actuators: (a) top view; and (b) view in a cross-section perpendicular to the streamwise direction.

An AC voltage at the frequency $f_{pa} = 4.2$ kHz was applied to the electrodes. To clarify the effects of the applied voltage on the control, it was changed in the range from $E_{pa} = 4$ kV_{p-p} to 5.5 kV_{p-p} in the experiments. Additionally, the effects of the pitch of the actuators, $s = 4, 10$ mm, and the spanwise width of the lower electrode, $d_1 = 1, 3, 5, 7$ mm, on the control were investigated. Moreover, to clarify

the nature of the control on the cavity flow and tone, aeroacoustic simulations were performed, as well as flow measurements, both with and without control. An actuator with $E_{pa} = 5 \text{ kV}_{p-p}$, $s = 10 \text{ mm}$ ($s/L = 0.5$, $s/\theta = 71$), and $d_1 = 3 \text{ mm}$ was utilized at $U_0 = 30 \text{ m/s}$, where substantial reduction of the intense sound was achieved.

2.3.2. Flush-Mounted Plasma Actuators

To minimize the influence on the flow and on noise generation of the protrusion of the actuators from the wall, a flush-mounted actuator, with the dielectric layer embedded in the model, was utilized so that the protrusion was only the $18 \text{ }\mu\text{m}$ thickness of the upper electrode. In order to maintain the sharpness of the cavity edge, the actuator was set back from the upstream edge by a space of $0.1L$ in the upstream direction.

Figure 6 compares the sound-pressure levels, at the fundamental frequency, of the cavity flow both with and without the actuator; the difference was negligibly small. Consequently, this flush-mounted actuator does not affect the evaluation of control effects on the cavity tone obtained using the low-noise wind tunnel.

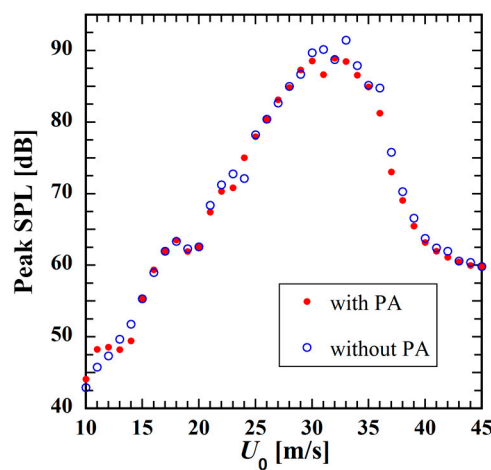


Figure 6. Comparison of the sound-pressure level SPL of the cavity flow both with and without a flush-mounted actuator.

2.4. Numerical Simulations

2.4.1. Governing Equations and Finite-Difference Schemes

To clarify the fluid-acoustic interactions in the cavity flows, the flow and acoustic fields were simultaneously simulated by solving the three-dimensional compressible Navier-Stokes equations with mass and energy conservation laws in conservation form:

$$\mathbf{Q}_t + (\mathbf{E} - \mathbf{E}_v)_x + (\mathbf{F} - \mathbf{F}_v)_y + (\mathbf{G} - \mathbf{G}_v)_z = \mathbf{D}, \quad (1)$$

$$\mathbf{D} = \begin{pmatrix} 0 \\ s_x(x, y, z, t) \\ s_y(x, y, z, t) \\ s_z(x, y, z, t) \\ D_c(s_x u + s_y v + s_z w) \end{pmatrix}, \quad (2)$$

where \mathbf{Q} is the vector of the conserved variables, \mathbf{E} , \mathbf{F} , \mathbf{G} are the inviscid flux vectors, and \mathbf{E}_v , \mathbf{F}_v , \mathbf{G}_v are the viscous flux vectors. To reproduce the body force produced by the actuator, the term \mathbf{D} representing the body force and the power added by it to the unit volume are included on the right-hand side of the equation [9]. Details of the body forces are described in next subsection.

The spatial derivatives were evaluated using a sixth-order-accurate, compact, finite-difference scheme (fourth-order accurate on the boundaries) [10]. Time integration was performed with a third-order-accurate Runge-Kutta method.

The flow in the cavity became turbulent under the given conditions, although the incoming boundary layer was laminar. To reduce the computational cost, large-eddy simulations (LES) were performed in the present study. No explicit subgrid-scale (SGS) model was used. The turbulent energy at the grid-scale (GS) that should be transferred to SGS eddies was dissipated by a 10th-order spatial filter described below. A number of studies [11–13] have shown that this approach, which combines low-dissipation discretization schemes with filtering, correctly reproduces turbulent flows. This filter, which also removes numerical instabilities, is given by [14]:

$$\alpha_f \hat{\psi}_{i-1} + \hat{\psi}_i + \alpha_f \hat{\psi}_{i+1} = \sum_{n=0}^5 \frac{a_n}{2} (\psi_{i+n} + \psi_{i-n}), \tag{3}$$

where ψ is a conserved quantity, and $\hat{\psi}$ is the filtered quantity. For the coefficients a_n , the same values as Gaitonde and Visbal [15] were utilized, and the value of the parameter α_f was set to be 0.45. Cavity flows with incoming laminar and turbulent boundary layers can be predicted with high accuracy using the methods described above [16].

2.4.2. Body Force Exerted by Plasma Actuators

The body force and the power exerted by the actuators were modeled by including the quantities s_x, s_y, s_z and $us_x + vs_y + ws_z$ in the Navier-Stokes equations. For the body-force vector, the expression as follows was used:

$$\begin{pmatrix} s_x \\ s_y \\ s_z \end{pmatrix} = A \rho_c(x, y, z) \begin{pmatrix} \varphi_x(x, y, z) \\ \varphi_y(x, y, z) \\ \varphi_z(x, y, z) \end{pmatrix} \sin^2(2\pi f_{pa} t), \tag{4}$$

$$A = 1 (\sin(2\pi f_{pa} t) \leq 0), -0.4 (\sin(2\pi f_{pa} t) > 0), \tag{5}$$

where ρ_c is the plasma density, and φ is the electric field. The square of the sine function in Equation (4) means that the plasma discharge occurs twice in one period, as in the body-force model of [9].

The distributions of plasma density and electric field were computed using the method proposed by Suzen [17]. In computing the plasma density, the Debye length was taken to be 0.7 mm, and the distributions of plasma density between the exposed upper electrodes were determined from the luminescence of the plasma.

Figure 7 shows the distributions of plasma density determined from the luminescence measurements along with those predicted near the wall ($y = 0.05$ mm), where the horizontal direction is the spanwise position from the midpoint of the embedded electrode ($z = z_{pa}$), which is non-dimensionalized using the pitch of the actuators. As shown in the figure, the predicted distributions agree well with those determined in the experiments.

The coefficient A in Equation (4) was introduced to represent the change of the amount and direction body forces between positive and negative applied voltages. The value of A was set to be the same as that in [18], where simulations by the above-described method were employed to reproduce the induced flow in an experiment by Forte [19].

The simulated distributions of the body forces are shown in Figure 8. The most intense body force is generated around the edges of the exposed electrodes. The non-dimensional maximum body force was taken to be $D_c = \rho_{c,max} E_{pa} / (\rho_0 U_0^2 / L) = 2.8 \times 10^{-6}$ so that control effects on the mean velocity profile in the cavity were in good agreement with those measured in the experiments discussed in Section 3.1.

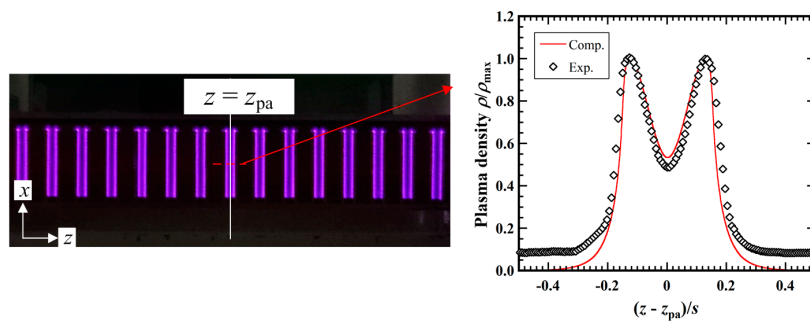


Figure 7. Plasma distributions. Photograph of the plasma luminescence (**left**). Predicted distributions of plasma density near the wall ($y = 0.05$ mm), compared with those determined from the plasma luminescence in the photograph (**right**).

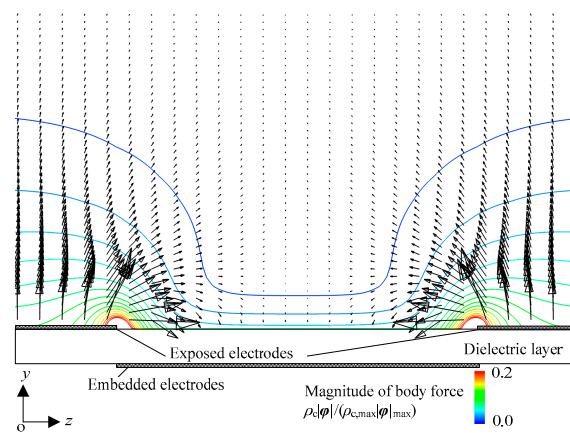


Figure 8. Predicted vectors of the body force and contours of the magnitude of the force vector.

2.4.3. Computational Grid

Figure 9 shows the computational grid for the flow over the cavity. The spanwise length $W_c/L = 3.0$ of the computational domain was sufficiently wide to reproduce the effects of control by an actuator with pitch $s/L = 0.5$, with six sets of electrodes included in the computation. The spanwise grid resolution was $\Delta z/L = 1/80$. The streamwise resolution in the cavity was $\Delta x/L = 1/100$, and the normal resolution near the wall in the incoming boundary layer and in the shear layer in the cavity was $\Delta y_{\min}/L = 1/400$. The grid was stretched into the far field in both the normal and streamwise directions. The grid resolution in the x - y cross-section in the cavity was the same as that in our past research [8], where the predicted flow and sound fields were found to be in good agreement with those measured. The total number of grid points was 55 million.

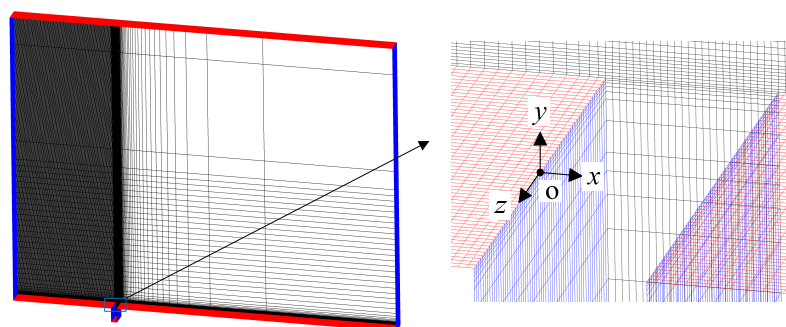


Figure 9. Computational grid, where every fourth grid line is shown for clarity.

2.4.4. Boundary Conditions

Figure 10 shows the boundary conditions. Non-reflecting boundaries [20–22] at the inflow and outflow boundaries were utilized so that acoustic waves pass the boundaries smoothly. On the lower boundary at the upstream side of the cavity, the boundary condition was changed from a slip wall to a non-slip and adiabatic wall. The position of this change was determined so as to make the thickness of the incoming boundary layer equal to that measured. Periodic boundary conditions were used in the spanwise direction. A uniform steady flow was asymptotically imposed in the inflow buffer region ($x/L \leq -12.5$).

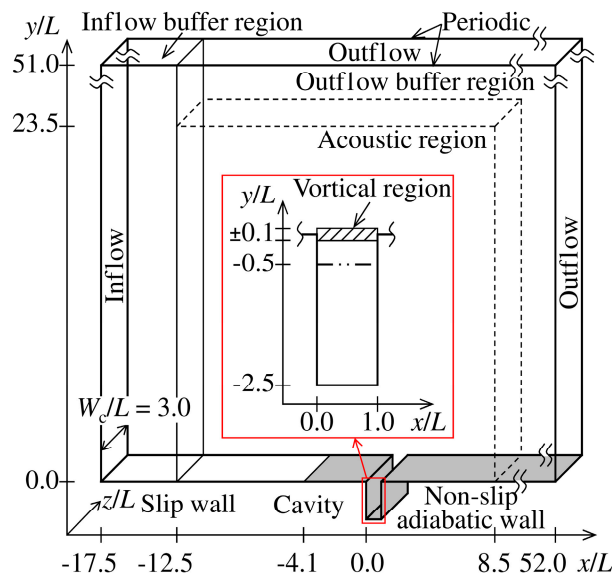


Figure 10. Computational domain and boundary conditions.

2.4.5. Prediction of the Far Acoustic Field

The porous Ffowcs, Williams, and Hawkins (FW-H) method [23–25] was used to predict the acoustic pressure at the measurement point ($x/L = 6.75$ and $y/L = 21.5$). The pressure p was sampled at a semi-cylindrical surface of radius $r = 2.5L$, near the center of the cavity ($x/L = 0.5$ and $y = 0$).

A spanwise computational domain of width $W_c = 3L$, which was chosen to be smaller than that of the experiment, $W = 7.5L$, was utilized in order to reduce computational resources. To take the effects of this difference into account, the sound-pressure levels, $SPL(f)$, were corrected by using the equivalent coherence length, $L_c(f)$, which was computed based on the coherence of the velocity along the center of the cavity ($x/L = 0.5, y = 0$) in the spanwise direction. The detailed method is described in [5].

3. Comparison and Validation

3.1. Flow Fields

Figure 11a shows a visualization of the induced flow in the y - z cross-section produced by activating the actuators in the absence of a freestream flow. As shown in the figure, a pair of vortices with a streamwise (x) axis are induced by each actuator, composed of two upper electrodes and one lower electrode. Figure 11b shows the predicted velocity vectors color-coded by the vertical velocity component under the same conditions. The streamwise vortices measured in the experiments also occur in the present simulation. The predicted maximum induced velocity was roughly 2 m/s.

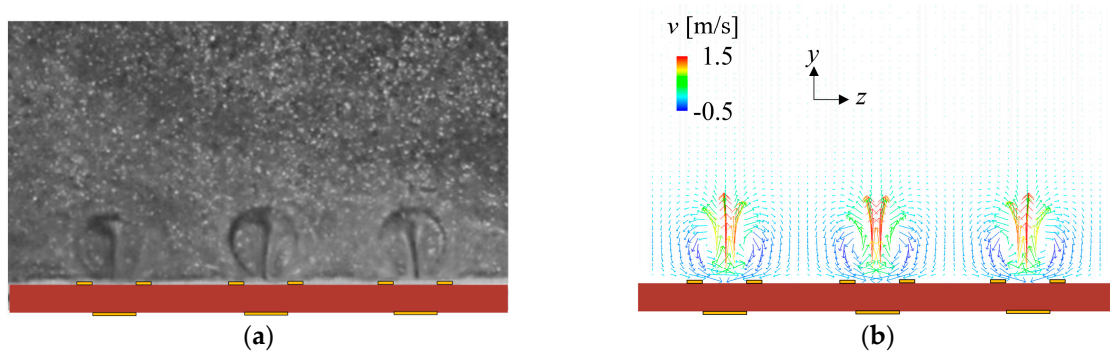


Figure 11. Vortices induced by actuators in the absence of a freestream flow: (a) visualized flow in the experiment; and (b) the predicted velocity vectors color-coded by values of the vertical velocity.

The predicted mean velocity profiles at the position $x/L = 0.05$ and $z = z_{pa}$ for $U_0 = 30$ m/s, both with and without control are compared with those measured. The time-series velocity, measured by the hot-wire anemometer in our experiment, was given by $u_h = (u^2 + [0.5v]^2)^{0.5}$ in the computation, in the same way as in our previous research [26], and the time-averaged values, U_h , were computed. Figure 12 shows that the predicted profile agrees well with that measured for cases both with and without control. The free shear layer is moved in the upward direction by the control. This is because the incoming boundary is moved upward due to the streamwise vortices induced by the control.

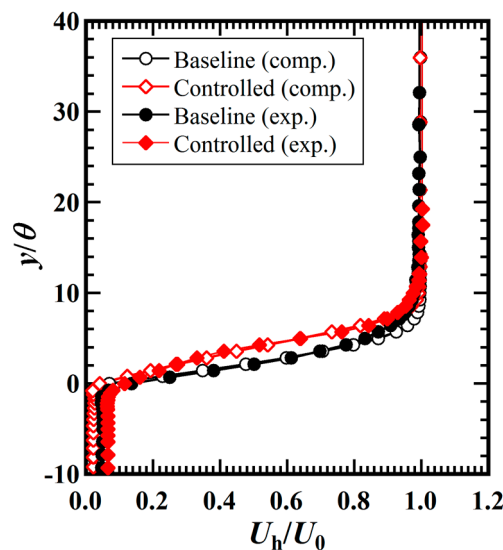


Figure 12. Predicted and measured mean velocity profiles with and without control ($x/L = 0.05$, $z = z_{pa}$).

3.2. Sound-Pressure Spectra

Figure 13 shows the measured and predicted sound-pressure spectra both with and without control, where the frequency resolution is $\Delta St = 0.1$ ($\Delta f = 156$ Hz), where St represents the Strouhal number based on the cavity length and the freestream velocity. The spectra were averaged 9374 and 18 times, respectively, in the experimental and computational results. The predicted fundamental frequency around $St = 1.0$ agrees well with that measured both with and without control. The sound-pressure level at the fundamental frequency also is in good agreement with that measured, both with and without control, where the level is reduced by the control. The predicted and measured reduction levels were 5 and 6 dB, respectively.

The discussions in the previous and present subsections confirm that the present computations adequately predict the flow and sound fields, both with and without control.

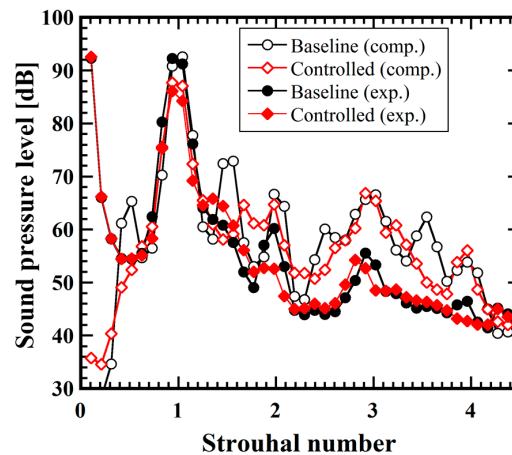


Figure 13. Predicted and measured sound-pressure spectra, both with and without control.

4. Results and Discussions

4.1. Measured Geometric Effects of Actuators on Control

The variation of the sound-reduction level at the fundamental frequency of 1500 Hz as a function of the voltage E_{pa} applied to the actuators was measured, where the spanwise pitch of the lower electrode was either $s = 4$ mm or $s = 10$ mm, and the fixed width of the lower electrode was $d_1 = 3$ mm. Figure 14a shows the measured variation. The frequency resolution of spectral analysis was $\Delta f = 4.88$ Hz and it should be noted that the reduction level was different from that in the previous section due to the difference of the frequency resolution.

As shown in Figure 14a, the amount of noise reduction is greater for higher applied voltages, particularly in the range from $E_{pa} = 4$ kV_{p-p} to 5.5 kV_{p-p}. The sound level drops sharply at lower voltages for the narrower pitch $s = 4$ mm, as compared to the case with $s = 10$ mm. For $s = 4$ mm, the sound reduction level of 31 dB was achieved at $E_{pa} = 5$ kV_{p-p}. However, for a fixed cavity width, more actuators and greater power consumption are necessary for narrower pitches. In the next subsection, the sound-reduction mechanism is discussed for $s = 10$ mm and $E_{pa} = 5.0$ kV_{p-p}.

According to the investigation by Yokoyama et al. [5], the cavity tone was also reduced by pairs of introduced streamwise vortices by blowing jets in the incoming boundary layer. Additionally, the results at the jet velocity of $V_j/U_0 = 0.07$, which roughly corresponds to the jet velocity (2 m/s) induced by the present plasma actuators, show that the control effects became smaller for finer spanwise displacement of the jets, such as $s/L = 0.1$ and 0.25. The maximum reduction level was achieved at $s/L = 0.5$. This was because the induced longitudinal vortices were weakened for the finer displacement.

Meanwhile, the present plasma actuators can most largely reduce cavity tone with a finer displacement of $s/L = 0.2$. This difference from the results of blowing jets is possibly because the electrodes of the actuators are elongated into the streamwise direction making it easier to introduce intense streamwise vortices, while the blowing jets were ejected from simple circular holes. Deliberately SETTING up the inlet shape and blowing direction for the jets for the introduction of the streamwise vortices possibly increases the effects.

The comparison of the present results with those of the control by blowing jets indicates that the present plasma actuators can effectively introduce longitudinal vortices and reduce cavity tone with a finer displacement. Meanwhile, for a fixed cavity width, more actuators and greater power consumption are necessary for a narrower displacement. The exact estimation of power consumption remains a problem for the future.

To clarify the effects of the lower-electrode width on control of the cavity tone, the sound-reduction levels were measured for lower-electrode widths of $d_1 = 1, 3, 5,$ and 7 mm, at a constant pitch of

$s = 10$ mm, as shown in Figure 14b. The results show that sound reduction was obtained and that the influence of the lower-electrode width on sound reduction was small, except for the narrowest width, $d_1 = 1$ mm. Streamwise vortices are not induced at this narrow width, possibly because the body force is not sufficiently large, due to too narrow a width for expansion of the plasma between the exposed electrodes [27].

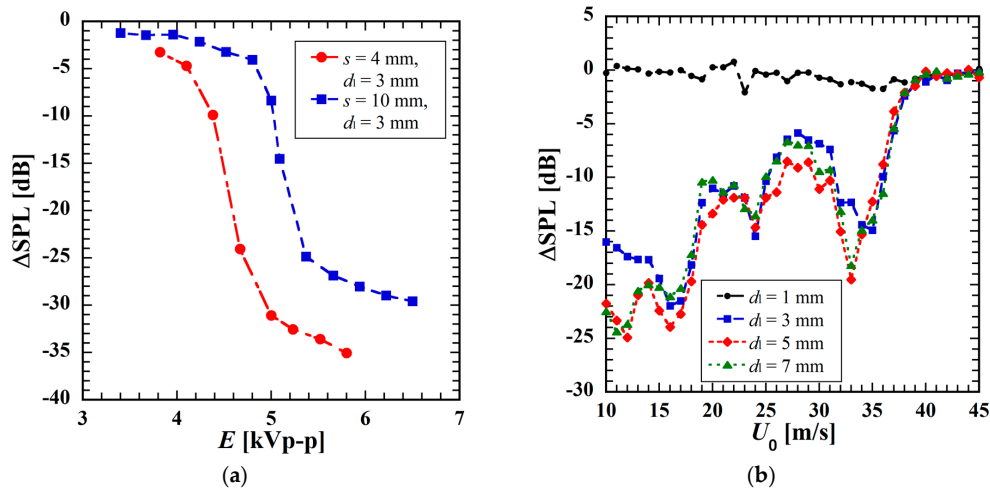


Figure 14. (a) The variation of the sound-reduction level, in decibels, at the fundamental frequency of 1500 Hz as a function of the applied voltage; and (b) the variation of the sound-reduction level for different lower-electrode widths as a function of the freestream velocity U_0 .

4.2. Control Effects on Flow Structures and Pressure Fields

4.2.1. Vortical Structures

Figure 15 shows the predicted vortical structures with and without control as iso-surfaces of the second invariant $q \equiv ||\Omega||^2 - ||S||^2$, where Ω and S are the anti-symmetric parts and symmetric parts, respectively, of the velocity gradient tensor for the phase-averaged flow fields at the phase where the vortex collides with the downstream edge of the cavity. The iso-surfaces are color-coded by the values of the streamwise vorticity.

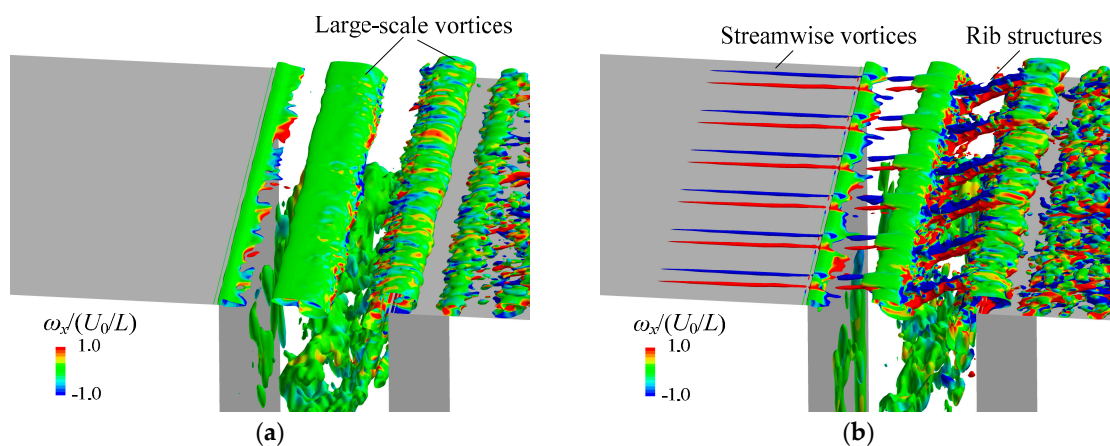


Figure 15. Iso-surfaces of the second invariant of $q/(U_0/L)^2 = 0.45$ color-coded by values of the streamwise vorticity for phase-averaged flow fields at $U_0 = 30$ m/s at the phase where the vortex collides with the downstream edge of the cavity: (a) baseline flow; and (b) controlled flow.

As shown in Figure 15a, two-dimensional large-scale vortices are generated in the baseline cavity flow. Low-pressure regions are generated in the large-scale vortices, and an expansion wave is radiated due to the collision of the vortices with the downstream edge of the cavity [16]. Figure 15b shows that streamwise vortices are induced by the actuators in the incoming boundary layer and form rib structures between the large-scale vortices.

Figure 16 shows the iso-surfaces of the component of the second invariant q_z , which was computed from Equation (6):

$$q_z \equiv |\omega_z|^2 - \left\| \begin{pmatrix} S_{xx} & S_{yx} \\ S_{xy} & S_{yy} \end{pmatrix} \right\|^2, \quad q_z \equiv |\omega_z|^2 - \left\| \begin{pmatrix} S_{xx} & S_{yx} \\ S_{xy} & S_{yy} \end{pmatrix} \right\|^2, \quad (6)$$

where ω_z is the spanwise vorticity and S_{xx} , S_{xy} , and S_{yy} are the elements of the symmetric parts of the velocity gradient tensor. This quantity is related to vortices with spanwise axes and is color-coded by the spanwise vorticity in the figure. Figure 16 also shows the contours of streamwise vorticity in the shear layer ($y/\theta = 2.9$).

As shown in Figure 16a, vortical structures with spanwise axes are apparent in the baseline flow. These vortices correspond approximately to the above-mentioned large-scale vortices. The periodic collision of these vortices with the downstream edge of the cavity produces the intense cavity tone. Figure 16b shows that these vortices are distorted by the streamwise vortices in the controlled flow.

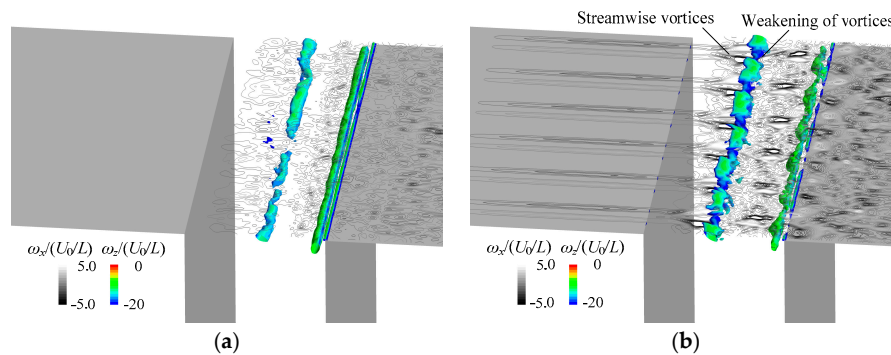


Figure 16. Iso-surfaces of the component of the second invariant related to vortices with a spanwise axis $q_z/(U_0/L)^2 = -20$ color-coded by the spanwise vorticity, together with contours of the streamwise vorticity in the shear layer ($y/\theta = 2.9$) at the phase where the vortex collides with the downstream edge of the cavity: (a) baseline flow; and (b) controlled flow.

4.2.2. Power Spectra of Velocity Fluctuations

Figure 17 shows the predicted power spectra of velocity fluctuations at $x/L = 0.5$ and $z = z_{pa}$ at the peak of maximum power for $y/\theta = 6.4$ and 3.6 , respectively, with and without control, along with the measured data. The figure shows that the power at the fundamental frequency is weakened by the control in both computations and experiments. This corresponds to the weakening of the above-mentioned large-scale vortices with spanwise axes that produce the cavity tone.

4.2.3. Spanwise Coherence

To clarify further the nature of the vortical structures, the coherence between two points separated by spanwise distances Δz at $x/L = 0.5$ and $y = 0$ was examined. Figure 18 shows the spanwise coherence of the streamwise velocity with and without control. Although the coherence shows locally-high values, depending on the pitch $s/L = 0.5$ of the actuators, overall it is decreased.

Figure 19 shows the phase-averaged fluctuation pressure with and without control at the phase where the vortex collides with the downstream edge of the cavity. In the baseline flow, the distribution of the pressure is coherent in the spanwise direction. At the collision of the large-scale vortical structures

with the downstream edge of the cavity, the radiated sound is reinforced in the spanwise direction by the coherent pressure fluctuations. In the controlled flow, however, the fluctuation pressure varies in the spanwise direction. This variation also contributes to the weakening of the cavity tone.

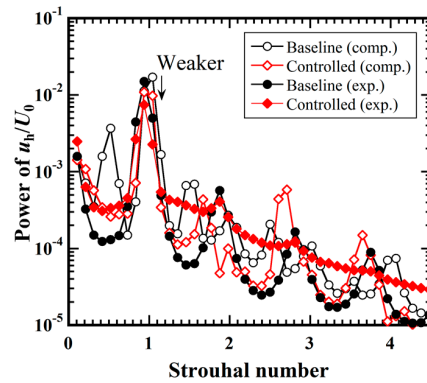


Figure 17. Predicted power spectra of velocity, u_h , with and without control at the peak of maximum power for $y/\theta = 6.4$ and 3.6 at $x/L = 0.5$ and $z = z_{pa}$, with and without control, respectively. The measured spectra at the peak of maximum power for $y/\theta = 5.7$ and 2.8 at the same streamwise and spanwise positions of $x/L = 0.5$ and $z = z_{pa}$ with and without control, respectively, are also shown.

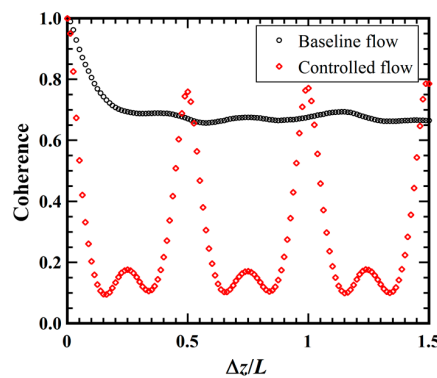


Figure 18. Spanwise coherence of streamwise velocity, u , at $x/L = 0.5$ and $y = 0$ for baseline and controlled flows.

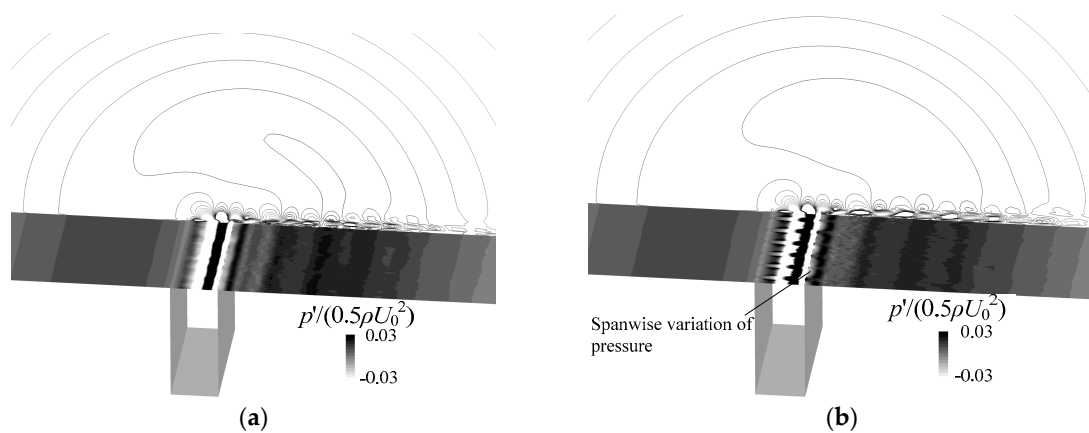


Figure 19. Contours of the fluctuation pressure at $U_0 = 30$ m/s for phase-averaged flow fields at the phase where the vortex collides with the downstream edge of the cavity: (a) baseline flow; and (b) controlled flow.

5. Conclusions

To clarify the mechanism by which streamwise plasma actuators aligned in the spanwise direction reduce the cavity tone with the acoustic resonances, direct aeroacoustic simulations were performed, as well as wind tunnel experiments. The predicted flow and acoustic fields, both with and without control, are in good agreement with those measured. To the authors' knowledge, this is the first time that direct aeroacoustic simulations of the control of aerodynamic noise by plasma actuators have been performed, including comparisons with experimental data.

On the measured effects of lower electrode width on the control, the cavity tone was effectively reduced for a lower-electrode width of $d_1 = 3, 5,$ and 7 mm, while the control effects on the cavity tone were negligible for $d_1 = 1$ mm. The predicted and measured flow fields show that streamwise vortices are induced by the actuators for $d_1 = 3$ mm in the absence of a freestream.

The results show that aerodynamic sound can be controlled at the relatively high freestream velocity of 30 m/s by 31 dB by plasma actuators with the spanwise fine pitch of actuators of $s = 4$ mm and $d_1 = 3$ mm at the applied voltage of $E_{pa} = 5$ kV_{p-p}, even though they can only induce flows with a maximum velocity of 2 m/s. In comparison with the control by blowing jets, the plasma actuators can more effectively reduce the cavity tone by introducing streamwise vortices with the fine displacement.

The predicted phase-averaged flow fields show that the streamwise vortices by the control are introduced into the cavity flow as longitudinal vortices. Due to these vortices, large-scale vortices with spanwise axes that cause the cavity tone are distorted and weakened. Moreover, the coherence of the velocity fluctuations in the spanwise direction decreases, which also contributes to the reduction of the cavity tone.

Although the exact estimation of the power consumption is a future problem, the effectiveness of the plasma actuators as the devices for noise reduction can be shown in this paper. The technological problems related with high-voltage safety or high-frequency effects are also remaining challenges for application to actual vehicles.

Acknowledgments: This work was supported by JSPS KAKENHI grant number JP17K06153 and through the application development for Post K computer (FLAGSHIP 2020) by the Ministry of Education, Culture, Sports, Science, and Technology of Japan (MEXT). The authors appreciate Mr. Kusumoto for contributions throughout the manufacturing of the actuators.

Author Contributions: Hiroshi Yokoyama conceived and designed the experiments, conducted the simulations, and wrote the paper; Isamu Tanimoto performed the experiments; Hiroshi Yokoyama and Isamu Tanimoto analyzed the data; Isamu Tanimoto contributed reagents/materials/analysis tools; and Hiroshi Yokoyama and Akiyoshi Iida supervised the research.

Conflicts of Interest: The authors declare no conflict of interest. The founding sponsors had no role in the design of the study; in the collection, analyses, or interpretation of data; in the writing of the manuscript, and in the decision to publish the results.

References

1. Rossiter, J.E. *Wind-Tunnel Experiments on the Flow over Rectangular Cavities at Subsonic and Transonic Speeds*; No. 3438; Ministry of Aviation: New Delhi, India, 1964. Available online: <http://naca.central.cranfield.ac.uk/reports/arc/rm/3438.pdf> (accessed on 7 July 2017).
2. Powell, A. On the edge tone. *J. Acoust. Soc. Am.* **1961**, *33*, 395–409. [CrossRef]
3. East, L.F. Aerodynamically induced resonance in rectangular cavities. *J. Sound Vib.* **1966**, *3*, 277–287. [CrossRef]
4. Zhuang, N.; Alvi, F.S.; Alkislar, M.B.; Shih, C. Supersonic cavity flows and their control. *AIAA J.* **2006**, *44*, 2118–2128. [CrossRef]
5. Yokoyama, H.; Adachi, R.; Minato, T.; Iida, A. Experimental and Numerical Investigations on Control Methods of Cavity Tone by Blowing Jet in an Upstream Boundary Layer. *SAE Int. J. Passeng. Cars Mech. Syst.* **2017**, *10*, 13–21. [CrossRef]
6. Huang, X.; Zhang, X. Streamwise and spanwise plasma actuators for flow-induced cavity noise control. *Phys. Fluids* **2008**, *20*, 037101. [CrossRef]

7. Gupta, A.D.; Roy, S. Noise control of subsonic cavity flows using plasma actuated receptive channels. *J. Phys. D* **2014**, *47*, 1–5. [[CrossRef](#)]
8. Yokoyama, H.; Odawara, H.; Iida, A. Effects of freestream turbulence on cavity tone and sound source. *Int. J. Aerosp. Eng.* **2016**, *2016*, 7347106. [[CrossRef](#)]
9. Kaneda, I.; Sekimoto, S.; Nonomura, T.; Asada, K.; Oyama, A.; Fujii, K. An effective three-dimensional layout of actuation body force for separation control. *Int. J. Aerosp. Eng.* **2012**, *2012*, 786960. [[CrossRef](#)]
10. Lele, S.K. Compact finite difference schemes with spectral-like resolution. *J. Comput. Phys.* **1992**, *103*, 16–42. [[CrossRef](#)]
11. Rizzetta, D.P.; Visbal, M.R. Large-eddy simulation of supersonic cavity flow fields including flow control. *AIAA J.* **2003**, *41*, 1452–1462. [[CrossRef](#)]
12. Bogey, C.; Bailly, C. Large eddy simulations of round free jets using explicit filtering with/without dynamic Smagorinsky model. *Int. J. Heat Fluid Flow* **2006**, *27*, 603–610. [[CrossRef](#)]
13. Bogey, C.; Bailly, C. Turbulence and energy budget in a self-preserving round jet: Direct evaluation using large eddy simulation. *J. Fluid Mech.* **2009**, *627*, 129–160. [[CrossRef](#)]
14. Matsuura, K.; Kato, C. Large-eddy simulation of compressible transitional flows in a low-pressure turbine cascade. *AIAA J.* **2007**, *45*, 442–457. [[CrossRef](#)]
15. Gaitonde, D.V.; Visbal, M.R. Pade-type higher-order boundary filters for the Navier-Stokes equations. *AIAA J.* **2000**, *38*, 2103–2112. [[CrossRef](#)]
16. Yokoyama, H.; Kato, C. Fluid-acoustic interactions in self-sustained oscillations in turbulent cavity flows, I. Fluid-dynamic oscillations. *Phys. Fluids* **2009**, *21*, 105103. [[CrossRef](#)]
17. Suzen, Y.B.; Huang, P.G.; Jacob, J.D.; Ashpis, D.E. Numerical Simulations of Plasma Based Flow Control Applications. In Proceedings of the 35th Fluid Dynamics Conference and Exhibition, Toronto, ON, Canada, 6–9 June 2005; No. AIAA 2005-4633. pp. 1–11. [[CrossRef](#)]
18. Kusumoto, M.; Yokoyama, H.; Angland, D.; Iida, A. Control of aerodynamic noise from cascade of flat plates by plasma actuators. *Trans. JSME* **2017**, *83*, 16-00364. (In Japanese) [[CrossRef](#)]
19. Forte, M.; Jolibois, J.; Pons, J.; Moreau, E.; Touchard, G.; Cazalens, M. Optimization of a dielectric barrier discharge actuator by stationary and non-stationary measurements of the induced flow velocity: Application to airflow control. *Exp. Fluids* **2007**, *43*, 917–928. [[CrossRef](#)]
20. Thompson, K.W. Time dependent boundary conditions for hyperbolic systems. *J. Comput. Phys.* **1987**, *68*, 1–24. [[CrossRef](#)]
21. Poinso, T.J.; Lele, S.K. Boundary conditions for direct simulations of compressible viscous flows. *J. Comput. Phys.* **1992**, *101*, 104–129. [[CrossRef](#)]
22. Kim, J.W.; Lee, D.J. Generalized characteristic boundary conditions for computational aeroacoustics. *AIAA J.* **1987**, *38*, 2040–2049. [[CrossRef](#)]
23. Williams, J.E.F.; Hawkins, D.L. Sound generation by turbulence and surfaces in arbitrary motion. *Philos. Trans. R. Soc. A* **1968**, *264*, 321–342. [[CrossRef](#)]
24. Lyrintzis, A.S. Surface integral methods in computational aeroacoustics—From the (CFD) near-field to the (Acoustic) far-field. *Int. J. Aeroacoust.* **2003**, *2*, 95–128. [[CrossRef](#)]
25. Shur, M.L.; Spalart, P.R.; Strelets, M.K. Noise prediction for increasingly complex jets. Part I: Methods and tests. *Int. J. Aeroacoust.* **2005**, *4*, 213–246. [[CrossRef](#)]
26. Yokoyama, H.; Kitamiya, K.; Iida, A. Flows around cascade of flat plates with acoustic resonance. *Phys. Fluids* **2013**, *25*, 106104. [[CrossRef](#)]
27. Enloe, C.L.; McLaughlin, T.E.; VanDyken, R.D.; Kachner, K.D.; Jumper, E.J.; Corke, T.C.; Post, M.; Haddad, O. Mechanisms and Responses of a Single Dielectric Barrier Plasma Actuator: Geometric Effects. *AIAA J.* **2004**, *42*, 595–604. [[CrossRef](#)]

